Energies **2015**, *8*, 2312-2336; doi:10.3390/en8042312

OPEN ACCESS

energies

ISSN 1996-1073

www.mdpi.com/journal/energies

Article

Research on a Small Signal Stability Region Boundary Model of the Interconnected Power System with Large-Scale Wind Power

Wenying Liu, Rundong Ge, Quancheng Lv *, Huiyong Li and Jiangbei Ge

Electrical and Electronic Engineering Institute, Mailbox 435, North China Electric Power University, No. 2 Beinong Road, Changping District, Beijing 102206, China;
E-Mails: liuwenyingls@ncepu.edu.cn (W.L.); gerundong@126.com (R.G.); lihuiyong311@ncepu.edu.cn (H.L.); gejiangbei1205@163.com (J.G.)

* Author to whom correspondence should be addressed; E-Mail: lvquanchengncepu@126.com; Tel.: +86-152-1072-8746; Fax: +86-10-6177-3725.

Academic Editor: Paul Stewart

Received: 4 December 2014 / Accepted: 18 March 2015 / Published: 25 March 2015

Abstract: For the interconnected power system with large-scale wind power, the problem of the small signal stability has become the bottleneck of restricting the sending-out of wind power as well as the security and stability of the whole power system. Around this issue, this paper establishes a small signal stability region boundary model of the interconnected power system with large-scale wind power based on catastrophe theory, providing a new method for analyzing the small signal stability. Firstly, we analyzed the typical characteristics and the mathematic model of the interconnected power system with wind power and pointed out that conventional methods can't directly identify the topological properties of small signal stability region boundaries. For this problem, adopting catastrophe theory, we established a small signal stability region boundary model of the interconnected power system with large-scale wind power in two-dimensional power injection space and extended it to multiple dimensions to obtain the boundary model in multidimensional power injection space. Thirdly, we analyzed qualitatively the topological property's changes of the small signal stability region boundary caused by large-scale wind power integration. Finally, we built simulation models by DIgSILENT/PowerFactory software and the final simulation results verified the correctness and effectiveness of the proposed model.

Keywords: wind power; interconnected power system; catastrophe theory; small signal stability region boundary

1. Introduction

With the facts of fossil energy exhaustion and global ecology environment deterioration, wind power generation [1–3], as the most mature and effective renewable energy technology, is developing rapidly all over the world. In particular, China plans to construct nine ten-million kilowatt wind power bases [4,5] and parts of these bases have been put into operation. After these large-scale wind farms were put into operation, the large-scale wind power and traditional power system were connected to each other, sending out wind-thermal-bundled [6,7] power, which has become the typical operation mode of the power system. However, the current structure of the wind power transmission grid is still not strong enough to satisfy the scale of wind power integration. Thus, small signal stability has become the bottleneck restricting the sending-out of large-scale wind power as well as the transmission capacity of the power grid. To maintain the stability margin of the power grid, wind farms may even need to cease power production frequently. Thus, it is necessary to research the small signal stability of power grids with large-scale wind power integration.

Some [8–10] have studied the small signal stability of power systems with wind power integration so far. Generally speaking, however, most of this research is limited to a certain grid and typical working conditions, which is not a universal situation and may even yield conflicting results. The study of the small signal stability region boundary has broader perspectives and shows all the critical operating points of the small signal stability, which provides a more scientific and reasonable basis for the safety monitoring, defense and control of power systems.

In theory, the small signal stability region boundary [11,12] consists of saddle node bifurcation (SNB), Hopf bifurcation (HB) and singularity induced bifurcation (SIB). Among them, HB [13,14], which physically represents a pair of conjugate eigenvalues crossing the imaginary axis, is related to the system oscillatory instability. This paper mainly focuses on stability region boundary consisting of Hopf bifurcations.

At present, some papers also report research on the small signal stability region boundary. Seydel [15], Roose *et al.* [16] and Hiskens [17] studied the methods for obtaining the small signal stability region boundary based on a direct method and a continuation method, respectively. Sun and Yu [18] proposed fitting a boundary consisting of Hopf bifurcations using hyper-planes. Based on an implicit function, Yang *et al.* [19] presented a method to obtain the small signal stability region boundary through polynomial approximation. Jia *et al.* [20,21], and Li *et al.* [22] studied the influences on the small signal stability region boundary of exciter voltage limits, time delays and saturated links, respectively. Generally, these works were mainly focused on quickly finding the small signal stability region boundary of the traditional power system and the influences of various factors on the small signal stability region boundary, without paying attention to the boundary of the interconnected power system with large-scale wind power. Besides, most of the research methods in these papers are just massive calculations and iterations based on the electromagnetic model of the power system, unable to directly

provide enough information to reveal the topological properties of the small signal stability region boundary on the whole. In fact, for the interconnected power system with large-scale wind power, the small signal stability region boundary is still determined by the eigenvalue. From the perspective of the eigenvalues' changes, under certain conditions, a pair of complex eigenvalues may turn into real eigenvalues or from the opposite direction [23,24]. This phenomenon that the eigenvalues' change under critical conditions essentially shows obvious catastrophe indications and it's a kind of typical catastrophe phenomenon. Catastrophe theory [25–27] is often used in systems with obvious catastrophe indications. A significant advantage of catastrophe theory is that it can establish a functional relationship between control variables and state variables without contacting any special inner mechanism to avoid solving differential equations of the whole power system. At present, catastrophe theory has been widely applied in road traffic [28], biology [29], geotechnical engineering [30], and sociology [31], but seldom in power systems. Sallam and Dineley [32], and Wvong and Mihiring [33,34] studied the dynamic stability and transient stability of power systems based on catastrophe theory. Mahmoud [35] used catastrophe theory to analyze the voltage stability of a distribution network and proposed some new voltage indexes. Yusheng *et al.* [36] set up a cusp catastrophe model for over-heating faults of oil-immersed transformers and further proposed a remaining life prediction method for this kind of transformer. However, catastrophe theory has no application in small signal stability or other related wind power research as of yet. Hence, this paper establishes the small signal stability region boundary model of an interconnected power system with large-scale wind power based on catastrophe theory and the catastrophe indications of the eigenvalues.

The paper is organized as follows: the first section, as a preface, expounded the current situation of the research and problems studied in this paper. The second section analyzed typical characteristics and mathematical models of the interconnected power system with large-scale wind power. The third section discussed the disadvantages of traditional analysis methods of small signal stability region boundary. Section 4 introduced the basic principles of catastrophe theory. Section 5 analyzed the catastrophe indications of eigenvalues to apply catastrophe theory to the analysis of eigenvalues. Section 6 established the small signal stability region boundary model of interconnected power system with large-scale wind power in two-dimensional power injection space and extend the 2D model to multi dimensions. In Section 7, simulations were conducted to verify the model. In the end, we summarized our work of this paper.

2. An Interconnected Power System with Large-Scale Wind Power and Its Model

2.1. Interconnected Power System with Large-Scale Wind Power and Its Typical Characteristics

Due to that wind power resources in China are centralized and far from the load centers, wind power development always uses the manner of centralized development and long-distance transportation. For now, China is planning to construct nine ten-million kilowatts wind power bases in Gansu, Xinjiang, Hebei *etc.*, which are connected to the traditional power system and together form the interconnected power system with large-scale wind power. These systems show some visible characteristics as follows: the capacity of wind power is much larger than that of the local loads which makes it hard for it to be consumed on site; wind farms cover large areas and the power of each wind farm is transmitted into a

higher voltage power grid after collection at power collection points through transmission lines; wind power needs long distance lines to be sent out; wind power bases are always located together at the end of the power grid and the outward power delivery structure is relatively weak, which results in serious stability problems, *etc*. Figure 1 shows the Jiuquan wind power base and its outward power transmission channels.

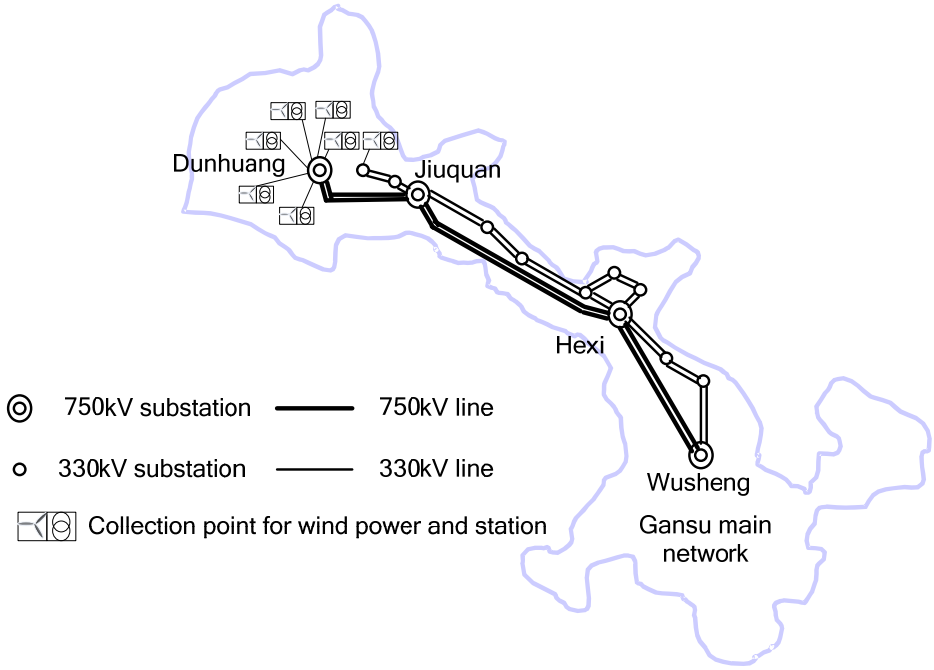

Figure 1. Outward power transmission channels of Jiuquan wind power base.

2.2. Equivalence of Large-Scale Wind Power Base

In the interconnected power system with large-scale wind power, a wind power base is composed of a large number of wind farms, covering a large area. Thus, wind power from the same area is always collected at certain HV bus power collection points and then sent out at a higher voltage class through a transformer. For example, the first-stage project of Jiuquan wind power base, mainly located in Yumen and Guazhou, forms nine power collection points, including seven 330 kV booster stations and two 330 kV substations. The wind power is then sent out through a 750 kV line.

The wind farms of the same power collection point include large numbers of wind turbines, so it is impossible to establish different models for each wind turbine. On the other hand, the power output of these wind turbines show similar change trends [7] and the wind turbines have similar states when large amounts of wind is available. Therefore, it's feasible to establish an equivalent model to simulate the operation of a wind farm group. That is to say, regard the power collection point as a unit and replace the wind farms of the same power collection point by an equivalent wind turbine, which specifically comes down to two steps: firstly, replace *m* wind turbines of the same wind farm by one equivalent wind turbine adopting the capacity weighted method [37]. The calculation of the parameters of the equivalent wind turbine is shown in Equation (1):

$$\begin{cases} S_{eq}=\sum_{i=1}^{m}S_i,\ P_{eq}=\sum_{i=1}^{m}P_i,\ Q_{eq}=\sum_{i=1}^{m}Q_i \\ x_{m-eq}=\sum_{i=1}^{m}\frac{S_i}{S_{eq}}x_m,\ x_{s-eq}=\sum_{i=1}^{m}\frac{S_i}{S_{eq}}x_s,\ x_{r-eq}=\sum_{i=1}^{m}\frac{S_i}{S_{eq}}x_r \\ r_{s-eq}=\sum_{i=1}^{m}\frac{S_i}{S_{eq}}r_s,\ r_{r-eq}=\sum_{i=1}^{m}\frac{S_i}{S_{eq}}r_r \\ H_{eq}=\sum_{i=1}^{m}\frac{S_i}{S_{eq}}H_i,\ K_{eq}=\sum_{i=1}^{m}\frac{S_i}{S_{eq}}K_i,\ D_{eq}=\sum_{i=1}^{m}\frac{S_i}{S_{eq}}D_i \end{cases} \quad (1)$$

In Equation (1), subscript m is the total number of wind turbines in a wind farm. Subscript i is the number of wind turbines. Subscript eq means equivalent parameters. x_m is the magnetizing reactance, x_s and r_s represent the reactance and resistance of the stator circuit respectively, x_r and r_r represent the reactance and resistance of the rotor circuit respectively, the units of which are Ω. S is the capacity of the wind turbine in MVA. P is the active output of the wind turbine in MW. Q is the reactive output in Mvar. H is the inertia time constant in s. K represents the shafting stiffness coefficient in N·m/rad. D is the shafting damping coefficient in s.

After the wind farm is made equivalent to one wind turbine, each power collection point will connect several equivalent wind farms. A typical sending-out model of wind power at the same power collection point is shown in Figure 2.

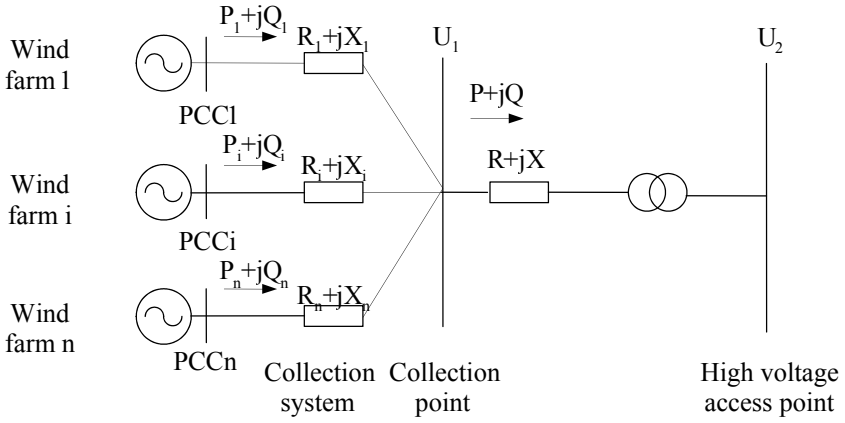

Figure 2. Typical sending-out model of wind power.

In Figure 2, $P_i + jQ_i$ is the output power of wind farm i. The PCC bus of each wind farm is connected to the collection bus through the transmission line whose impedance is $R_i + jX_i$, and the collection point is connected to the high voltage access point through the transmission line whose impedance is $R + jX$ and the transformer.

For the typical system with wind power sending-out in Figure 2, with the same method, several equivalent wind turbines of the same power collection point were replaced by another equivalent wind turbine. For the collection system, an equivalent power loss method was adopted, assuming that different wind farms have the same voltage U. The voltage of the equivalent wind farm is also U and $R_\Sigma + jX_\Sigma$ represents the impedance of the equivalent collection system, thus:

$$\sum_{i=1}^{n}\frac{(P_i^2+Q_i^2)}{U^2}(R_i+jX_i)=\frac{\sum_{i=1}^{n}(P_i^2+Q_i^2)}{U^2}(R_\Sigma+jX_\Sigma) \tag{2}$$

Then we obtain:

$$\begin{cases} R_\Sigma=\dfrac{\sum_{i=1}^{n}(P_i^2+Q_i^2)R_i}{\sum_{i=1}^{n}(P_i^2+Q_i^2)} \\ X_\Sigma=\dfrac{\sum_{i=1}^{n}(P_i^2+Q_i^2)X_i}{\sum_{i=1}^{n}(P_i^2+Q_i^2)} \end{cases} \tag{3}$$

So far, we have replaced the wind farm group of the same power collection point with an equivalent wind turbine. Because a wind power base always consists of limited power collection points, we replace the base with a group of wind turbines. Now, the typical structure of interconnected power system with large-scale wind power is as shown in Figure 3.

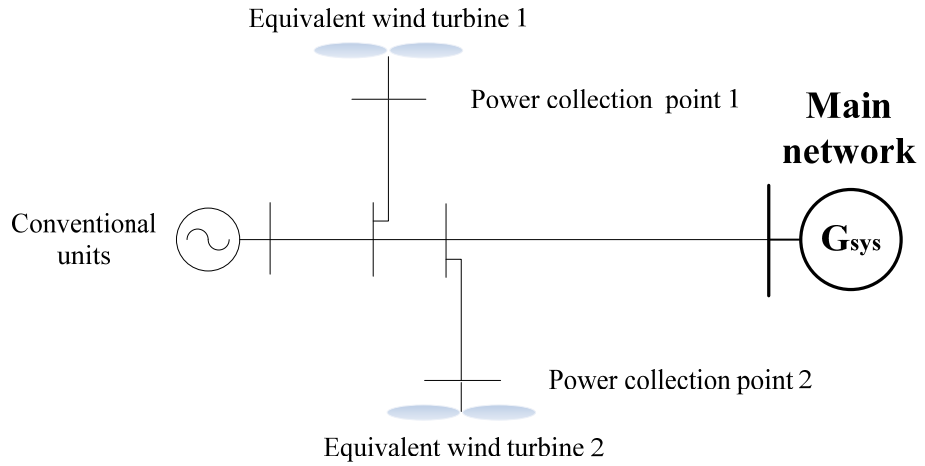

Figure 3. Typical structure of interconnected power system with large-scale wind power.

2.3. Model of Interconnected Power System with Large-Scale Wind Power

For the interconnected power system with large-scale wind power, the dynamic elements including the wind turbine can be expressed as a set of differential algebraic equations [38,39]:

$$\begin{cases} \dot{x}_i=f_i(x_i,u_i) \\ i_i=g_i(x_i,u_i) \end{cases} \tag{4}$$

In Equation (4), x_i is state variable of each dynamic element; u_i is the terminal voltages of each dynamic element; i_i is the current injected into the network.

Collecting all of these equations of dynamic elements we obtain a set of differential algebraic equations of an interconnected power system with large-scale wind power:

$$\begin{cases} \dot{x} = f(x,u) \\ i = g(x,u) \end{cases} \tag{5}$$

where x is the state variable vector of the power system; u is the vector of the bus terminal voltage; i is the current vector injected into the bus; f and g are nonlinear differential equations composing of f_i, g_i.

In Equation (5), the current i and voltage u follow the basic principle of the circuit:

$$i = Y_n u \tag{6}$$

where Y_n is the network admittance matrix. Equations (5) and (6) together form the model of an interconnected power system with large-scale wind power.

3. Traditional Analysis Method of Small Signal Stability Region Boundary and Its Disadvantage

In the traditional analysis method, we establish a state matrix to acquire the small signal stability region boundary based on the model of the power system. Concrete steps are as follows:

Equation (5) can be linearized as Equation (7) at the equilibrium point:

$$\begin{cases} \Delta\dot{x} = A_D \Delta x + B_D \Delta u \\ \Delta \mathrm{i} = C_D \Delta x + Y_D \Delta u \end{cases} \tag{7}$$

where $A_D = \partial f/\partial x$, $B_D = \partial f/\partial u$, $C_D = \partial g/\partial x$, $Y_D = \partial g/\partial u$; Δx is the micro-increment of x; Δu is the micro-increment of u and Δi is the micro-increment of i.

From Equation (6) we obtain:

$$\Delta i = Y_n \Delta u \tag{8}$$

Substituting Equation (8) into Equation (7) we can reach Equation (9) after rearranging:

$$\Delta\dot{x} = [A_D + B_D (Y_N - Y_D)^{-1} C_D]\Delta x = A\Delta x \tag{9}$$

The eigenvalues of the system state matrix A will decide whether the system reaches the small signal stability region boundary under some critical conditions: (1) SNB occurs when a pair of real eigenvalues cross the imaginary axis; (2) HB occurs when a pair of complex conjugate eigenvalues cross the imaginary axis; (3) SIB occurs when $(Y_N - Y_D)$ is singular. These three kinds of bifurcation form the small signal stability region boundary $\partial\Omega_{sssr}$:

$$\partial\Omega_{sssr} = \{\mathrm{SNBs}\} \mathrm{U} \{\mathrm{HBs}\} \mathrm{U} \{\mathrm{SIBs}\} \tag{10}$$

where SNBs is the point set of SNB, HBs is the point set of HB, SIBs is the point set of SIB.

The key to analyzing the small signal stability region boundary is figuring out when the parameters of the power system reach a critical condition. Conventional methods acquire the boundary by continuous adjustment of the system parameters and calculating the eigenvalues of the system state matrix. Because of the huge order and complex coupling properties of the power system model, conventional methods are trapped in complicated calculations and lack enough information to directly reveal the topological properties of the small signal stability region boundary on the whole.

In contrast, based on catastrophe theory, we can directly establish a function between control variables and state variables without contacting any special inner mechanism, thus avoiding solving the

differential equations of the whole system and making it very applicable to the analysis of systems with an unknown or difficult to obtain inner mechanism. Nevertheless, catastrophe theory itself has inherent drawbacks. On one hand, in a practical complex system, it's difficult to establish its potential function through derivation. On the other hand, catastrophe theory is mainly applied to systems with no more than five control variables. However, this does not affect the application of catastrophe theory in this paper. Thus we adopt catastrophe theory to discuss the model of the small signal stability region boundary of interconnected power systems with large-scale wind power.

4. Catastrophe Theory

Catastrophe theory was first proposed in 1972 by Thom, a French mathematician. This theory held that system dynamics can be derived through a smooth potential and critical points can be classified according to potential function [27].

The form of the system potential function is as follows:

$$f: V(X \times C) \tag{11}$$

where X is the state variable vector $(x_1, x_2, \ldots, x_n)$; C is the control variable vector $(c_1, c_2, \ldots, c_r)$ which represents r independent control variables. The equilibrium surface M, which is a subset of $R^n \times R^r$ space, represents the system's stable operating points, defined as Equation (12):

$$V'(x) = 0 \tag{12}$$

where superscript "′" represents the derivation of x for V. The definition of singularity set S is a subset of M consisting of all degenerate critical points of V, namely:

$$V''(x) = 0 \tag{13}$$

Mapping S to the control space C, then we obtain the bifurcation set B which is the control parameter set when catastrophe happens to the system's operating state. The bifurcation set B can be obtained by combing Equations (12) and (13) to eliminate the state variable vector X. Appendix A shows a typical catastrophe mechanism explaining the principle of catastrophe theory.

Thom's proof [25,36] indicated that the property of the potential function was not decided by state variables but the number of control variables. Generally, when the number was no more than four, there were only seven different kinds of catastrophe. Table 1 shows different potential functions of these seven basic kinds of catastrophe, where x, y are state variables and v, μ, w, t are control variables.

Table 1. Elementary catastrophe models and their potential functions.

Catastrophe model	Potential functions
Fold	$V(x) = x^3 + vx$
Cusp	$V(x) = x^4 + \mu x^2 + vx$
Swallowtail	$V(x) = x^5 + \mu x^3 + vx^2 + \omega x$
Butterfly	$V(x) = x^6 + tx^4 + \mu x^3 + vx^2 + \omega x$
Elliptic	$V(x, y) = x^3 - xy^2 + w(x^2 + y^2) + \mu x + \upsilon y$
Hyperbolic	$V(x, y) = x^3 + y^3 + \omega xy + \mu x + \upsilon y$
Parabolic	$V(x, y) = y^4 + x^2y + wx^2 + ty^2 + \mu x + \upsilon y$

5. Eigenvalue Catastrophe Indications

Catastrophe theory is often used in systems with obvious catastrophe indications. The catastrophe indications [26,27,36] are certain obvious characteristics of a catastrophe system including catastrophe, multi-modes and divergence, *etc*. Among them catastrophe is the most basic and obvious catastrophe indication, indicating some sudden change of the system state; multi-modes means that the number of the system states may be more than one; divergence shows the instability of the path perturbation of control parameters. Usually, a small perturbation of control parameters usually only causes small changes of the state variables except the perturbation near the degenerate critical point, which may causes huge changes in the final value of state variables.

Small signal stability is decided by the eigenvalues of the system. From the perspective of the change of eigenvalues, under some certain conditions, a pair of complex eigenvalues may turn into real eigenvalues or from the opposite direction, which is a typical kind of catastrophe phenomenon remarkably similar to changes of the equations' roots in Appendix A. This process also shows multi-mode characteristics. In addition, a small perturbation of parameters near the critical point would cause huge changes in the properties of the eigenvalues, thus showing the typical characteristics of divergence. Therefore, a change of eigenvalues indicates obvious catastrophe indications and shows that the use of catastrophe theory is both feasible and reasonable.

There are two kinds of application of catastrophe theory to specific problems, which are the analysis method and the empirical method. The analysis method is deducing where the equilibrium position of dynamical system is, while the empirical method establishes a system catastrophe model according to system external characteristics with mathematical descriptions of the unknown bifurcation set. It builds equilibrium surface equations of the system by data fitting or qualitative fitting [26,27] and chooses an appropriate catastrophe model according to the number of control variables and state variables.

6. Small Signal Stability Region Boundary Model of the Interconnected Power System with Large-Scale Wind Power

Hopf bifurcation is related to the system oscillatory instability and this paper mainly focuses on the stability region boundary consisting of Hopf bifurcations. Here, we established the small signal stability region boundary model of the interconnected power system with large-scale wind power in two-dimensional power injection space and extend the 2D model to multiple dimensions to obtain the small signal stability region boundary model in multidimensional power injection space.

6.1. Small Signal Stability Region Boundary Model in Two-Dimensional Power Injection Space

In this paper, we assumed power sources 1 and 2 were any two power sources, which can influence the dominant oscillation mode and their type were wind power or conventional power units. We choose a large unit which is far from and unrelated to the dominant oscillation mode as the system balancing machine. Keeping the structure and parameters of the system unchanged and at the same time keeping the node power injected unchanged except for the balancing machine, then active power injected by source 1 and 2 forms a two-dimensional small signal stability region boundary.

Essentially, this boundary is decided by the system eigenvalues. Because the analysis method involves complex nonlinear differential equations, this paper adopts the empirical method to establish the catastrophe model. We choose P_1, the active power of source 1 and P_2, the active power of source 2 as control variables and the eigenvalues of the dominant oscillation mode as state variable x. There are two control variables and one state variable in total, corresponding to the cusp catastrophe model in Table 1.

In catastrophe theory, the potential function is expanded according to a Taylor series abandoning high-order terms and simplifies the model by differentiable homeomorphism. The simplest model is called a canonical form [25] such as the potential functions in Table 1. The differentiable homeomorphism of the cusp catastrophe model only involves linear transformation [25], so the differences between each parameter and the canonical form of the cusp catastrophe model are no more than a coefficient and a constant, that is:

$$V(x) = a(x - x_0)^4 + b(P_1 + c)(x - x_0)^2 + (P_2 + d)(x - x_0) \tag{14}$$

where a, x_0, b, c, d are unknown constants. The formulation of equilibrium surface is as follows:

$$V'(x) = 4a(x - x_0)^3 + b(P_1 + c)(x - x_0) + P_2 + d = 0 \tag{15}$$

Hopf bifurcation is the operating point of the equilibrium surface and the state variable in accord to the Hopf bifurcation point is $x = 0 \pm jn$. Substitute $x = 0 \pm jn$ into Equation (15) and we obtain:

$$\begin{cases} -4ax_0^3 + 12an^2x_0 - (4an^2 - 12ax_0^2)x_0 + P_2 + d = 0 \\ b(P_1 + c) + 6ax_0^2 - 2an^2 = 0 \end{cases} \tag{16}$$

After arranging Equation (16):

$$\begin{cases} P_1 = \dfrac{2a}{b}n^2 - \dfrac{1}{b}(bc + 6ax_0^2) \\ P_2 = -8ax_0n^2 - 8ax_0^3 - d \end{cases} \tag{17}$$

By eliminating variable n we get:

$$e_{12}P_1 + e_{21}P_2 = f_{12} \tag{18}$$

where:

$$\begin{cases} e_{12} = 4x_0b \\ e_{21} = 1 \\ f_{12} = -(d + 4bcx_0 + 32ax_0^3) \end{cases} \tag{19}$$

Here e_{12} and f_{12} are both constants. According to Equation (18), P_1 and P_2 show a linear change relationship on the small signal stability region boundary. Equation (18) is the small signal stability region boundary model of the interconnected power system with large-scale wind power in two-dimensional power injection space. We can determine the small signal stability region boundary according to e_{12} and f_{12} acquired by data fitting.

It needs to be indicated that Hopf bifurcations is not the bifurcation set B of catastrophe theory. The bifurcation set B corresponds to catastrophe points of the catastrophe model. However, the catastrophe

point of the catastrophe theory in fact represents a sudden jump of the properties of eigenvalues, including complex eigenvalues turning into real eigenvalues or real eigenvalues turning into complex eigenvalues while Hopf bifurcation represents eigenvalues crossing the imaginary axis. The comparison sketch between Hopf bifurcation and catastrophe point is shown in Figure 4.

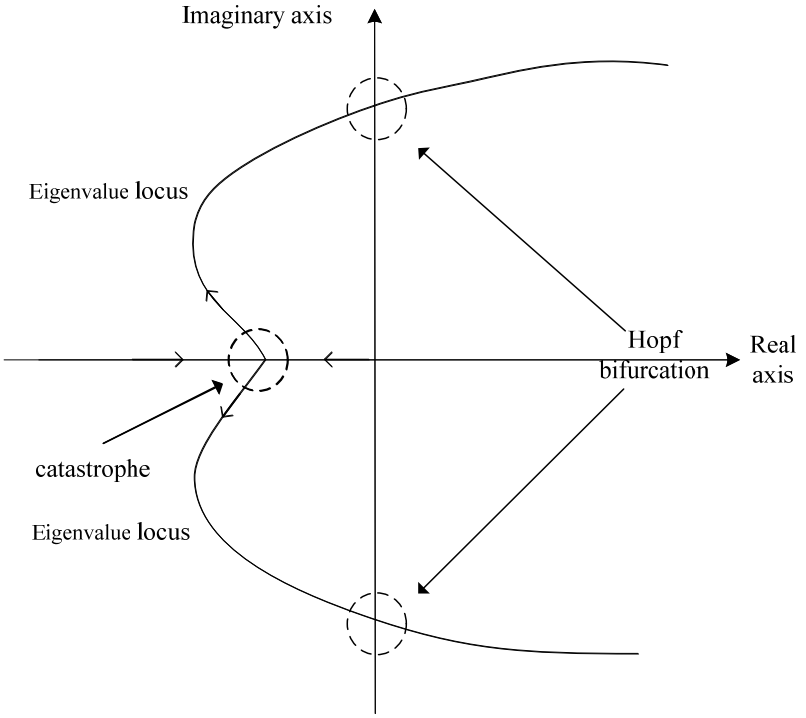

Figure 4. The comparison sketch between Hopf bifurcation and catastrophe point.

This difference should not discourage the application of catastrophe theory. The potential function of catastrophe theory is expanded according to a Taylor series and abandons unnecessary high-order terms, which is a standard technique in catastrophe theory. Catastrophe theory provides a rigorous proof [25] and truncation to make this approach has a reliable foundation. Thus, the potential function obtained in this way still has enough accuracy for all the operating points of the system. The equilibrium surface equation consists of the derived functions is also widely valid and applicable. That is to say, the equilibrium surface equations are still reasonable for Hopf bifurcation.

6.2. Small Signal Stability Region Boundary Model in Multidimensional Power Injection Space

Based on the two-dimensional boundary model, this section deduced the small signal stability region boundary model in multidimensional power injection space. Assume power source 1, 2, …, *n*, which can influence the dominant oscillation mode and their type are wind power or conventional power units. These *n* power sources can form these two-dimensional boundaries as Equation (20) shows:

$$\begin{cases} e_{12}P_1+e_{21}P_2=f_{12} & \{P_3,P_4,\cdots P_n \ \text{constant}\} \\ e_{13}P_1+e_{31}P_3=f_{13} & \{P_2,P_4,\cdots P_n \ \text{constant}\} \\ \cdots\cdots\cdots\cdots & \\ e_{1n}P_1+e_{n1}P_n=\mathrm{f}_{1n} & \{P_2,P_3,\cdots P_{n-1} \ \text{constant}\} \end{cases} \tag{20}$$

Arrange Equation (20) and make the coefficient of P_1 to be 1and we get:

$$\begin{cases} P_1+\dfrac{e_{21}}{e_{12}}P_2=\dfrac{f_{12}}{e_{12}} & \{P_3,P_4,\cdots P_n \ \text{ constant}\} \\ P_1+\dfrac{e_{31}}{e_{13}}P_3=\dfrac{f_{13}}{e_{13}} & \{P_2,P_4,\cdots P_n \ \text{ constant}\} \\ \cdots\cdots\cdots\cdots & \\ P_1+\dfrac{e_{n1}}{e_{1n}}P_n=\dfrac{f_{1n}}{e_{1n}} & \{P_2,P_3,\cdots P_{n\text{-}1} \ \text{ constant}\} \end{cases} \tag{21}$$

When their outputs change synchronously, these n sources form an n-dimensional boundary as Equation (22) shows:

$$k_1P_1 + k_2P_2 + \cdots + k_iP_i \cdots + k_nP_n = r \tag{22}$$

where k_1, $\cdots$, k_i, $\cdots$, k_n, and r can be constants as well as functions. Then make the coefficient of P_1 to be 1 and we get:

$$P_1+\frac{k_2}{k_1}P_2+\cdots+\frac{k_i}{k_1}P_i+\cdots+\frac{k_n}{k_1}P_n=\frac{r}{k_1} \tag{23}$$

For P_1 and P_i ($i \in \{2, \cdots, n\}$), keep the other power injection in Equation (23) fixed to obtain Equation (24):

$$P_1+\frac{k_i}{k_1}P_i=\frac{r}{k_1}-\frac{k_2}{k_1}P_{20}-\cdots-\frac{k_{i\text{-}1}}{k_1}P_{(i-1)0}-\frac{k_{i+1}}{k_1}P_{(i+1)0}-\cdots-\frac{k_n}{k_1}P_{n0} \tag{24}$$

Subscript 0 represents fixed value. According to Equation (21), the relationship between P_1 and P_i is linear, with a slope of e_{i1}/e_{1i}. To make Equation (24) satisfy the relationship in Equation (21), we kept $k_i/k_1 = e_{i1}/e_{1i}$.

Because i represents any number of $\{2, \cdots, n\}$, we obtain $k_2/k_1 = e_{21}/e_{12}$, $\cdots$, $k_n/k_1 = e_{n1}/e_{1n}$. All of the coefficients above are constants. For Equation (24), r/k_1 must be constant, or else the right side of Equation (24) will be variable and fail to satisfy the linear relationship in Equation (21).

Therefore, coefficients in Equation (22) are determined:

$$P_1 + e_2P_2 + \cdots + e_iP_i \cdots + e_nP_n = f \tag{25}$$

where, $e_2 = e_{21}/e_{12}$, $\cdots$, $e_n = e_{n1}/e_{1n}$. e_2, $\cdots$, e_n; f are all constants.

Equation (25) is the small signal stability region boundary model in multidimensional power injection space. We can determine the small signal stability region boundary according to the coefficients of variables acquired by data fitting.

Sun and Yu [18] proposed a method to fit the small signal stability region boundary using a hyper-plane but lacked theories to support their arguments. However, the research in this paper provides theoretical support for their proposal.

In the analysis above, this paper never limits the type of power source, so large-scale wind power injection doesn't change the form of the small signal stability region boundary model but only changes the dimensions of the hyper-plane and the values of the parameters. When wind power is injected into system instead of common units, both the number of power sources and the dimensions of the

hyper-plane will remain unchanged. However, values of the parameters will change because the difference between properties of wind power and common units is very big. Wind power injection into a certain node in the power system makes the number of power sources increase, leading to changes of the parameters as well as the dimension of hyper-plane.

7. Simulation Verification

To verify the validity of the small signal stability region boundary model proposed in this paper, we tested two examples below.

7.1. Example 1

We built the simulation system shown in Figure 5 using DIgSILENT/PowerFactory software, where bus D is an infinite bus, buses A, B, C are respectively connected to normal generators G_1 with excitation system, DFIG wind farm 1 and DFIG wind farm 2. The capacity of wind farm 1 and wind farm 2 are 210 MVA and 300 MVA, respectively. Both of these wind farms consist of several sets of DFIG with the same parameters and operation conditions in parallel. In the analysis, each wind farm is equivalent to a wind turbine. We chose the 2 MW wind turbine built into the DIgSILENT/PowerFactory software as the wind turbine model and Hansen *et al.* [39] introduced the model in detail. Appendix B shows the parameters of each element in the system(Table B1 shows the parameters of one single DFIG; Table B2 shows the parameters of generator G_1; Table B3 shows the parameters of the excitation system equipped on G_1; Appendix B4 shows the parameters of the transmission lines.).

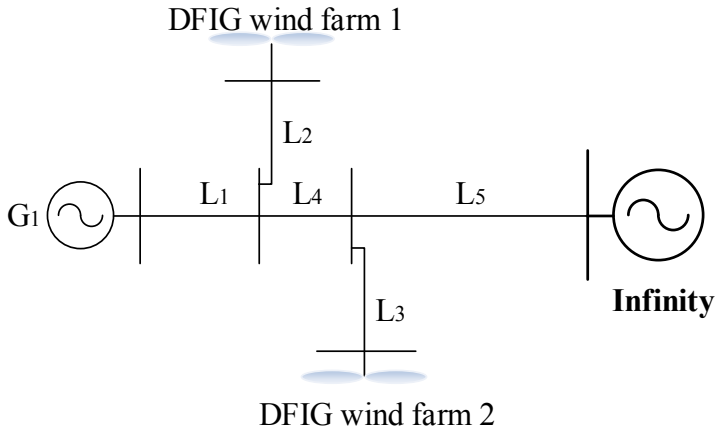

Figure 5. The wire map of the power system.

7.1.1. Test of the Two-Dimensional Boundary Model

Assume that P_1 is the active power of G_1, P_2 is the active power of wind farm 1 and P_3 is the active power of wind farm 2. Every power source operates with unity power factor. Keep P_3 = 200 MW and adjust the values of P_1 and P_2. When Hopf bifurcation occurs, take a sample of the data. Table C1 of Appendix C shows the sampling points.

Substitute the data in Table C1 into Equation (18) and obtain e_{12} = 1.3616, f_{12} = 413.1675, that is:

$$1.3616P_1 + P_2 = 413.1675 \quad (26)$$

Figure 6 shows the comparison between sampling points and the fitting boundary, where P_1 is the abscissa and P_2 is the ordinate. According to Figure 6, they have good consistency. In order to accurately express the error between the sampling points and the fitting boundary, define the error σ as follows:

$$\sigma = \frac{d}{\sqrt{P_1^2 + P_2^2}} \tag{27}$$

where d is the distance from sampling points to the fitting boundary. After calculation, we obtained that the average error was 0.319% and the biggest was 0.645%, which had good accuracy and showed that the model was reasonable and feasible. Detailed errors are shown in Table C2 of Appendix C.

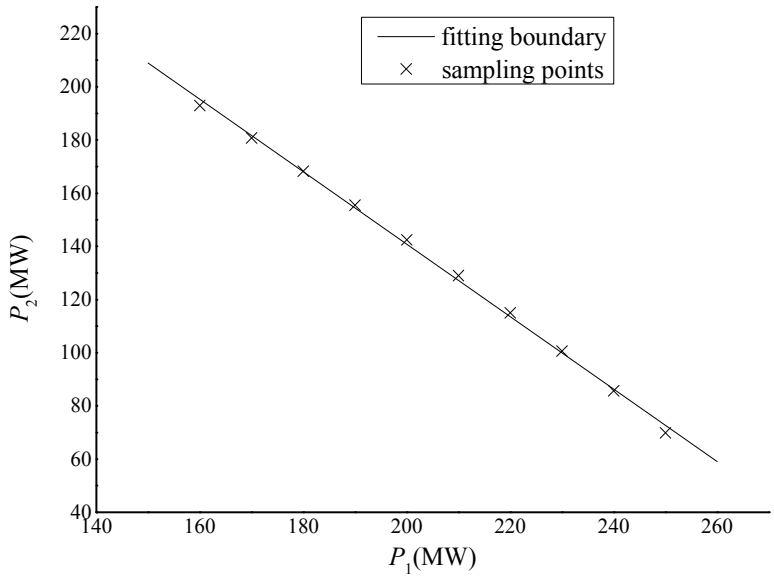

Figure 6. The two-dimensional stability region boundary contrast figure.

7.1.2. Verification of the Multidimensional Boundary Model

Every power source operates with unity power factor and we adjusted P_1, P_2 and P_3. When Hopf bifurcation occurs, take a sample of the data. Table C3 in Appendix C shows the sampling points.

Substitute the data in Table C3 into Equation (25) and obtain $e_2 = 0.7339$, $e_3 = 0.5871$, $f = 421.2902$, that is:

$$P_1 + 0.7339P_2 + 0.5871P_3 = 421.2902 \tag{28}$$

Figure 7 shows the contrast between sampling points and the fitting plane, where P_1, P_2, P_3 are three axes. According to Figure 7, they have good consistency.

In order to accurately express the error between sampling points and the fitting boundary, define the error σ as follows:

$$\sigma = \frac{d}{\sqrt{P_1^2 + P_2^2 + P_3^2}} \tag{29}$$

where d is the distance from sampling points to the fitting plane. After calculation, we obtained that the average error was 0.088% and the biggest was 0.18%, which had good accuracy and showed that the model was reasonable and feasible. Detailed errors are shown in Table C4 of Appendix C.

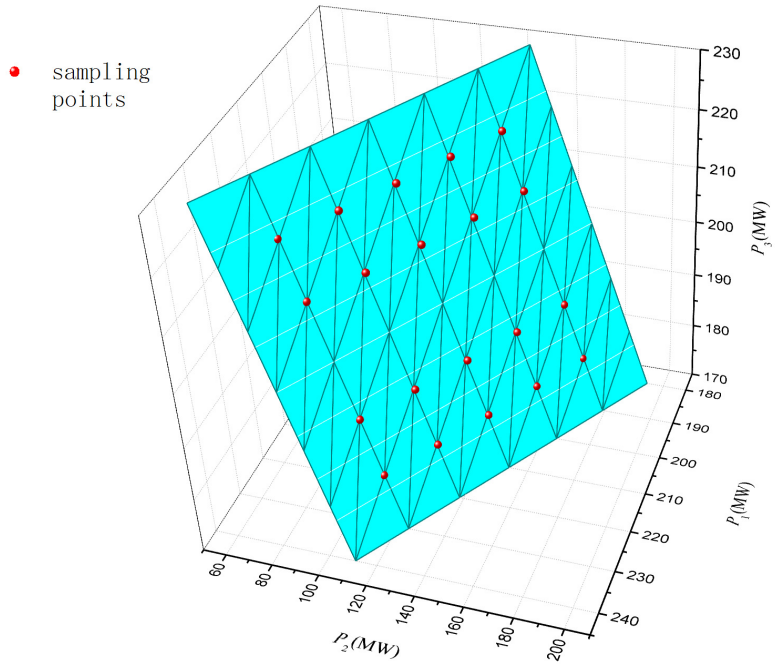

Figure 7. The three-dimension stability boundary contrast figure.

To make further analysis of the boundary, assume $P_3 = 200$ MW and turn Equation (28) into:

$$1.3626P_1 + P_2 = 414.0485 \quad (30)$$

This is the boundary equation degenerating into two dimensions. The difference between Equations (26) and (30) is very small, showing that the theory is reasonable and feasible.

7.1.3. Time-Domain Simulation Verification

To further test the accuracy of the boundary, we choose two operating points near the boundary: point 1 (210, 139, 180) and point 2 (210, 150, 180) and observe the stability of the system affected under a small disturbance by adopting time-domain simulation. Operating point 1 was in the boundary while point 2 was out of the boundary. The small disturbance was set as the mechanical torque's increasing 0.01 p.u of generator G_1 at 1 s, then restoring to the original level at 2 s. The simulation time was set at 50 s. Under the above disturbance, the power angle swing curves of generator G_1 at operating point 1 and point 2 were shown in Figure 8.

As can be seen from Figure 8, the swing amplitude of the angle at operation point 2 becomes larger and larger and the system would finally lose stability; while at operation point 1, the swing amplitude of the angle showed a decreasing trend and finally was stable. Thus, the time-domain simulation results also verified the validity of our theory on the stability boundary.

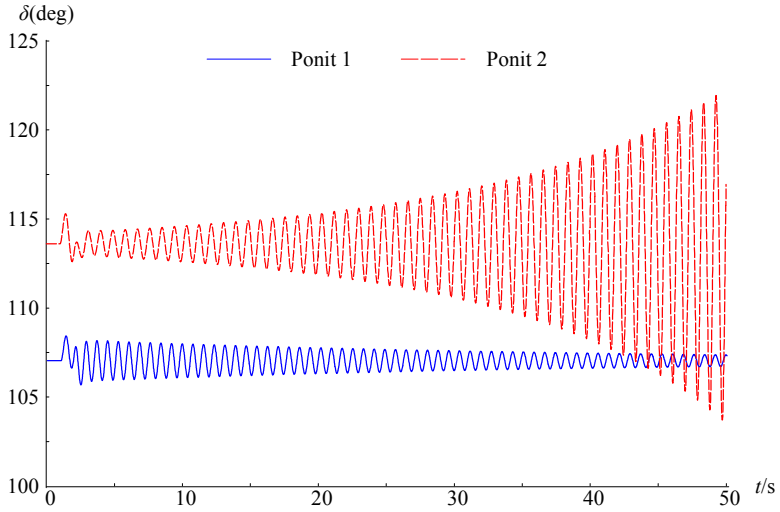

Figure 8. The angle swing curves of generator G1 at operation point 1 and point 2.

7.2. Example 2

The second simulation test uses the improved three generators and nine buses system. The length of each line in the IEEE three generators and nine buses system [40] is extended to 220% of the original value. Active power of load A (Figure 9) is set at 200 MW, load B at 250 MW, and load C at 200 MW. The remaining values stay unchanged. The DFIG wind farm 1 and wind farm 2 are connected to BUS7 and BUS9, respectively, through transformers. The system with the wind farm connected to it is shown in Figure 9.

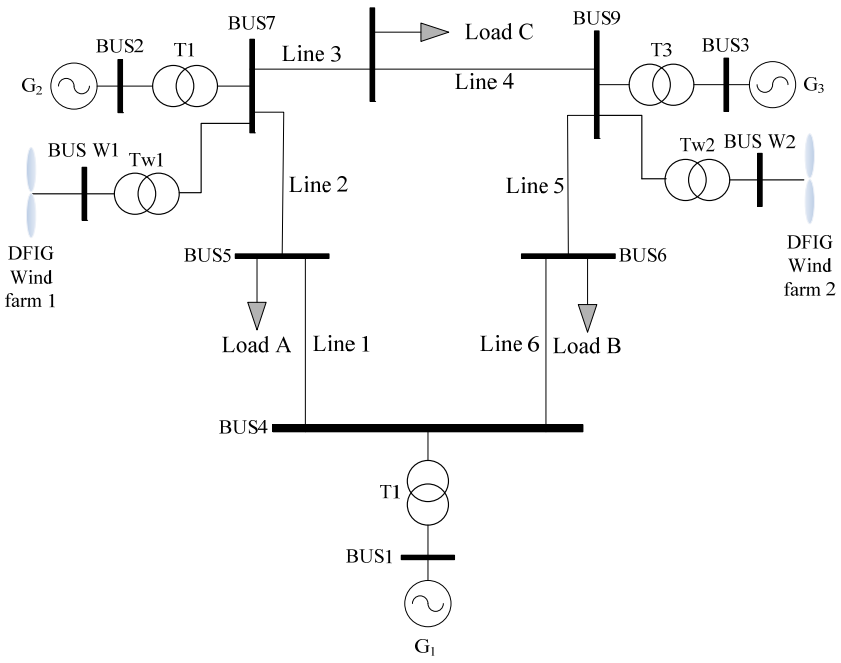

Figure 9. The improved model diagram of the three generators and nine buses system.

New equipment in this system include DFIG wind farm 1, DFIG wind farms 2, transformer Tw1, transformer Tw2, bus BUS W1, and bus BUS W2. Among them, DFIG wind farm 1 and 2 are both equivalent wind farms with a capacity of 150 MVA. Each single wind turbine still uses the 2 MW wind

turbine model in the DIgSILENT/PowerFactory in the equivalence. The parameters of the transformers Tw1 and Tw2 are shown in Table 2. The system was modeled by DIgSILENT/PowerFactory software.

Table 2. New transformer parameters.

Transformer	Rated voltage (kV)	Rated power (MVA)	Short-Circuit voltage U_k (%)	No-Load current I_0 (%)	Connection type
Tw1, Tw2	20/0.69	166.65	5	3	YN/yn0

There are two oscillation modes in the improved system. The frequency of one mode is around 1.15 HZ and the other is around 0.2 HZ. The 0.2 HZ mode has a strong damping in any case and the corresponding eigenvalues are far away from HB. Thus the paper does not consider this situation and mainly focuses on the 1.15 HZ mode.

Mark the active output of conventional unit G_2 as P_1, the active output of DFGI wind farm 1 as P_2, the active output of conventional unit G_3 as P_3 and the active output of DFGI wind farm 2 as P_4. The new wind farms adopt the unity power factor operation mode. Set G_1 as the balance unit and G_2, G_3 as PV nodes. Adjust the value of P_1, P_2, P_3, P_4 and sample data when HB occurs. Table D1 in Appendix D shows the sampling points.

Substitute the data in Table D1 into Equation (25) and obtain $e_2 = 1.0542$, $e_3 = 0.8195$, $e_4 = 0.878$, $f = 489.563$. That is

$$P_1 + 1.0542P_2 + 0.8195P_3 + 0.878P_4 = 489.563 \tag{31}$$

Similarly, define the error as follows:

$$\sigma = \frac{d}{\sqrt{P_1^2 + P_2^2 + P_3^2 + P_4^2}} \tag{32}$$

In Equation (32), d is the distance between the sampling points and the plane. The average value of the error was calculated to be 0.0384% and the maximum error was 0.0843%, which was of high accuracy. Detailed errors are shown in Table D2 of Appendix D. The results of time domain simulation were similar to Figure 8 and it was unnecessary to go into detail. The simulation above also verified the multi-dimensional boundary model.

From the above analysis, the stability region boundary provides a critical stable operating range of the system. The shorter the distance between current operating point and stability region boundary is, the more likely it is the system will lose stability. Thus, when the operation point is close to the stability region boundary, we need to adjust the output of each power supply timely and make the system away from the boundary, in order to avoid oscillation and instability of the system.

8. Conclusions

This paper provides a new method of analysis of the small signal stability region boundary for an interconnected power system with large-scale wind power. Compared with conventional analysis methods, based on the external characteristic modeling method of the running track, catastrophe theory directly established a function between control variables and state variables without contacting any

special inner mechanism. Applying catastrophe theory, this paper established a small signal stability region boundary model consisting of Hopf bifurcations and drawn the following conclusions:

(1) The small signal stability region boundary model in two-dimensional power injection space is a straight line. When the other injected power doesn't change, the power from the two power sources influencing the dominant oscillation mode shows a linear relation between them.
(2) The small signal stability region boundary model in multidimensional power injection space is a hyper-plane. When the other injected power doesn't change, the power from sources influencing the dominant oscillation mode forms a hyper-plane.
(3) Compared with the conventional system, large-scale wind power integration doesn't change the form of the small signal stability region boundary model but only the dimensions of the hyper-plane and the values of the parameters.

This paper developed a deeper understanding of the small signal stability region boundary of the interconnected power system with large-scale wind power and also presented new ideas and methods for its study.

Acknowledgments

This work is supported by the project "Research of the Impact Mechanism on Self-organized Critical State by Large-scale Cluster Grid-connected Wind Power and Identification", funded by the National Science Foundation of China (51377053), and the project "The Research of Key Techniques of Loss Reduction in Power System Based on Load-Net-Source Coordinated Control", funded by Major Project of State Grid Corporation of China (52272214002).

Author Contributions

Wenying Liu contributed to design, directed, and made suggestions for the research. Rundong Ge contributed to analysis, writing, and interpretation of the research. Quancheng Lv and Huiyong Li made some suggestions and translated this article from Chinese to English. Jiangbei Ge also made suggestions for the research. All co-authors contributed to the writing of the final research article.

Appendices

Appendix A: A typical catastrophe mechanism explaining the basic principle of catastrophe theory, (Figure A1)

The process of this mechanism is very simple. Firstly, pick two nearly identical rubber bands and cut from thin cardboard a disk whose diameter is one unit. Push a drawing pin through the disc at a point Q near the circumference with the point of this pin upwards. Mount the disc on a suitable base by pushing a second pin through the center, O. Loop the two rubber bands over the pin at Q, and use a third drawing pin to fasten the other end of one of the rubber bands to a point R on the base, two units from O. The remaining end, P, is left free.

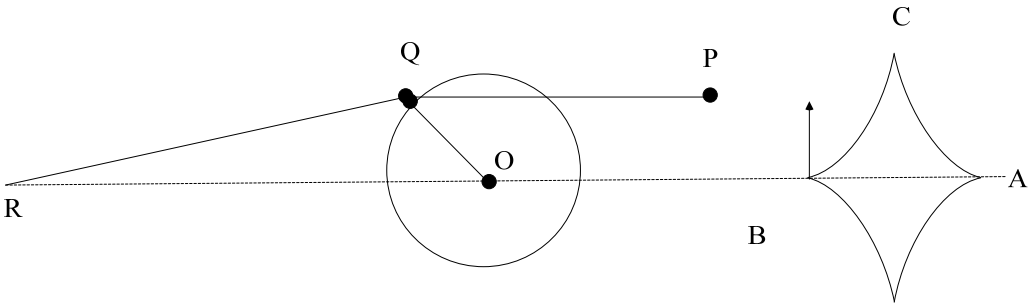

Figure A1. A typical catastrophe mechanism.

We operate the machine by moving P slowly in the plane of the machine. If we experiment for some time, we discover some curious features. The most obvious of these is that while the machine almost always responds smoothly to small changes in the position of P, is occasionally jumps suddenly. If we mark on the base the positions of P at which these jumps occur, we find that they form the perimeter of a curved diamond.

Saunders [25] made a detailed analysis of this sudden jump and turned the potential function of the mechanism into the following form:

$$V(x) = x^4 + \mu x^2 + vx \tag{A1}$$

That was the simplest model of the cusp catastrophe and the equilibrium surface was:

$$V'(x) = 4x^3 + 2ux + v = 0 \tag{A2}$$

Equation (A2) is a cubic equation, which has three real roots or just one real root. The literature [25] reveals that the mathematical essence of the sudden jump is changes in the real roots' number, namely a pair of complex roots turning into real roots or real roots turning into complex roots. The number of real roots was decided by the discriminant:

$$\Delta = 8u^3 + 27v^2 \tag{A3}$$

When $\Delta < 0$, there were three real roots; when $\Delta > 0$, there was only one real root, while $\Delta = 0$ was the critical condition of the changes of the number of real roots. It was easy to verify that $V'(x) = \Delta = 0$ was totally equivalent to $V'(x) = V''(x) = 0$, which was the bifurcation set B of the catastrophe system. Figure A2 shows the Equilibrium surface and bifurcation set of the cusp catastrophe model.

The equilibrium surface was divided into an upper lobe, middle lobe, and lower lobe. The bifurcation set B was the projection of two creases of the equilibrium surface on the *u*–*v* surface. If control variables changed to the bifurcation set B, there must be sudden jumps of equilibrium points (upper lobe jumped to lower lobe or lower lobe jumped to upper lobe). Obviously, the outline in Figure A1 is composed of the bifurcation set B in Figure A2.

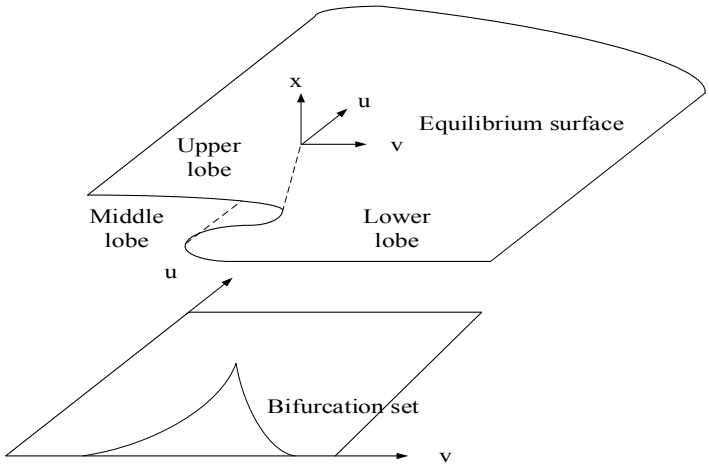

Figure A2. The Equilibrium surface and the bifurcation set of the cusp catastrophe model.

Appendix B

Appendix B1: DFIG Parameters

Table B1. DFIG parameters.

P_n (MW)	U_s (V)	R_s (p.u)	X_s (p.u)	X_m (p.u)	R_r (p.u)	X_r (p.u)	H_w (s)	H_g (s)	K
2	690	0.01	0.1	3.5	0.01	0.1	4.02	0.47	80.27

Appendix B2: Generator Parameters

Table B2. Generator parameters.

Generator	Capacity (WVA)	Voltage (KV)	x_d (p.u)	$x_d^{'}$(p.u)	x_q (p.u)	$x_q^{'}$(p.u)	$T_{d0}^{'}$(s)	$T_{q0}^{'}$(s)
G_1	300	18	1.72	1.66	0.23	0.378	0.8	0.12

The voltage and power reference values are this machine's rated voltage and capacity.

Appendix B3: Excitation Parameters

Details of the excitation system model refer to the A type exciter in Appendix B2 of reference [40]. The specific parameters are as follows:

Table B3. Excitation parameters.

τ_R	τ_{A1}	K_A	τ_{A2}	V_{Rmax}	V_{Rmin}	τ_E	K_E	K_F	τ_F	$E1$	$Se1$	$E2$	$Se2$
0.001	0.05	400	0.01	3	−3	0.95	−0.17	0.04	1	3.66	0.03	4.89	0.1

Appendix B4: Line Parameters

Line type is LGJ-400, L_1 of 60 km in length, L_2 of 30 km in length, L_3 of 30 km in length, L_4 of 30 km in length and L_5 of 100 km in length.

Appendix C

Table C1. The two-dimension boundary sampling points of small-signal stability region.

P_1 (MW)	P_2 (MW)	Real part	Imaginary part
160	192.95	−0.00002	7.371781
170	180.84	0.00001	7.42214
180	168.34	−0.00004	7.473076
190	155.49	0.00001	7.518541
200	142.43	−0.00003	7.544407
210	128.98	0	7.568171
220	115.07	0	7.593426
230	100.64	−0.00004	7.62154
240	85.64	0.00001	7.65214
250	69.94	0.00002	7.689427

Table C2. The errors of the two-dimension sampling points.

P_1 (MW)	P_2 (MW)	Error (%)
160	192.95	0.557664
170	180.84	0.204026
180	168.34	0.062567
190	155.49	0.247486
200	142.43	0.381506
210	128.98	0.419963
220	115.07	0.346774
230	100.64	0.151014
240	85.64	0.172708
250	69.94	0.644714

Table C3. The three-dimension boundary sampling points of small-signal stability region.

P_1 (MW)	P_2 (MW)	P_3 (MW)	Real part	Imaginary part
190	170.76	180	0.0001	7.536991
200	157.61	180	0	7.585456
210	144.3	180	−0.00002	7.610067
220	130.58	180	−0.00002	7.63315
230	116.39	180	−0.00001	7.656929
190	163.21	190	0	7.52991
200	150.12	190	−0.00002	7.565746
210	136.74	190	−0.00004	7.590114
220	122.94	190	0.00001	7.613221
230	108.64	190	0.00001	7.638675
190	147.67	210	0.00002	7.49535
200	134.54	210	0	7.520848
210	121	210	0.00003	7.545433
220	106.98	210	0.00003	7.572346
230	92.41	210	−0.00002	7.603393
190	139.64	220	0.00002	7.470371
200	126.43	220	0	7.496321

Table C4. The errors of the three-dimension sampling points.

P_1 (MW)	P_2 (MW)	P_3 (MW)	Error (%)
190	170.76	180	0.067958
200	157.61	180	0.013502
210	144.3	180	0.067639
220	130.58	180	0.051357
230	116.39	180	0.044867
190	163.21	190	0.008951
200	150.12	190	0.100204
210	136.74	190	0.141877
220	122.94	190	0.111855
230	108.64	190	0.002365
190	147.67	210	0.085745
200	134.54	210	0.16861
210	121	210	0.182398
220	106.98	210	0.116044
230	92.41	210	0.040263
190	139.64	220	0.079899
200	126.43	220	0.148584
210	112.78	220	0.144009
220	98.64	220	0.058873
230	83.92	220	0.119396

Appendix D

Table D1. The four-dimension boundary sampling points of small-signal stability region.

P_1 (MW)	P_2 (MW)	P_3 (MW)	P_4 (MW)	Real part	Imaginary part
164.25	130	90	130	0.00002	6.182942
162	130.11	93	130	−0.00005	6.135284
160	132	95	128.23	−0.00002	6.130719
155	135	92	133.33	−0.00009	6.108222
155	135	89	136.1	−0.00006	6.11538
150	139.94	90	135	−0.00012	6.123751
153.94	140	90	130	0.00003	6.195451
156.63	130	100	130	0	6.015732
155.96	130	90	140	0	6.026069
151	135	108	123.01	0.00001	5.995063
154.24	140	95	125	0.00001	6.186703
142.92	145	103	125	0.00005	6.069223
143.43	150	90	130	0.00003	6.213094
147	135	100	134.51	−0.00008	5.94512
152.053	130	105	130	0	5.92228
136	148.31	80	150	0.00013	6.061767
130.98	150	105	130	−0.00007	5.96777

Table D2. The errors of the four-dimension sampling points.

P_1 (MW)	P_2 (MW)	P_3 (MW)	P_4 (MW)	Error (%)
164.25	130	90	130	0.084283
162	130.11	93	130	0.019028
160	132	95	128.23	0.003579
155	135	92	133.33	0.033593
155	135	89	136.1	0.028496
150	139.94	90	135	0.040916
153.94	140	90	130	0.03755
156.63	130	100	130	0.031047
155.96	130	90	140	0.01475
151	135	108	123.01	0.042525
154.24	140	95	125	0.036604
142.92	145	103	125	0.065856
143.43	150	90	130	0.031106
147	135	100	134.51	0.050112
152.053	130	105	130	0.066951
136	148.31	80	150	0.001088
130.98	150	105	130	0.064887

Conflicts of Interest

The authors declare no conflict of interest.

References

1. Baños, R.; Manzano-Agugliaro, F.; Montoya, F.G.; Gil, C.; Alcayde, A.; Gómez, J. Optimization methods applied to renewable and sustainable energy: A review. *Renew. Sustain. Energy Rev.* **2011**, *15*, 1753–1766.
2. Hernández-Escobedo, Q.; Saldaña-Flores, R.; Rodríguez-García, E.R.; Manzano-Agugliaro, F. Wind energy resource in Northern Mexico. *Renew. Sustain. Energy Rev.* **2014**, *32*, 890–914.
3. Montoya, F.G.; Manzano-Agugliaro, F.; López-Márquez, S.; Hernández-Escobedo, Q.; Gil, C. Wind turbine selection for wind farm layout using multi-objective evolutionary algorithms. *Expert Syst. Appl.* **2014**, *41*, 6585–6595.
4. Li, J.F. *2012 China Wind Power Outlook*; China Environmental Science Press: Beijing, China, 2012; pp. 28–30. (In Chinese)
5. Kang, J.J.; Yuan, J.H.; Hu, Z.G.; Xu, Y. Review on wind power development and relevant policies in China during the 11th Five-Year-Plan period. *Renew. Sustain. Energy Rev.* **2012**, *16*, 1907–1915.
6. Chen, D.Z.; Ma, S.Y.; Song, Y.T.; Wang, N.B.; Fang, P.Y.; Ren, Y. Research on transient stability under HVDC block fault in wind-thermal-bundled power base transmitted by AC/DC system; In Proceedings of the 2014 International Conference on Power System Technology, Chengdu, China, 20–22 October 2014.
7. Xiao, C.Y.; Wang, N.B.; Ding, K.; Zhi, J. System power regulation scheme for jiuquan wind power base. *Proc. CSEE* **2010**, *30*, 1–7. (In Chinese)

8. Slootweg, J.G.; Kling, W.L. The impact of large scale wind power generation on power system oscillations. *Electr. Power Syst. Res.* **2003**, *67*, 9–20.
9. Mendonca, A.; Peas Lopes, J.A. Impact of large scale wind power integration on small signal stability. In Proceedings of the 2005 International Conference on Future Power Systems, Amsterdam, The Netherlands, 16–18 November 2005.
10. Gautam, D.; Vittal, V.; Harbour, T. Impact of increased penetration of DFIG-based wind turbine generators on transient and small signal stability of power systems. *IEEE Trans. Power Syst.* **2009**, *24*, 1426–1434.
11. Kwatny, H.G.; Fischl, R.F.; Nwankpa, C. Local bifurcation in power systems: Theory, computation and application. *Proc. IEEE* **1995**, *83*, 1453–1483.
12. Venkatasubramanian, V.; Schattler, H.; Zaborszky, J. Dynamics of large constrained nonlinear systems—A taxonomy theory. *Proc. IEEE* **1995**, *83*, 1530–1560.
13. Canizares, C.A.; Mithulananthan, N.; Milano, F. Linear performance indices to predict oscillatory stability problems in power systems. *IEEE Trans. Power Syst.* **2004**, *19*, 1104–1114.
14. Abed, E.H.; Varaiya, P.P.; Milano, F. Nonlinear oscillations in power systems. *Int. J. Electr. Power Energy Syst.* **1984**, *6*, 37–43.
15. Seydel, R. *Practical Bifurcation and Stability Analysis*, 3rd ed.; Springer: London, UK, 2010; pp. 199–257.
16. Roose, D.; Hlavacek, V. A direct method for the computation of Hopf bifurcation point. *SLAM J. Appl. Math*. **1985**, *45*, 879–894.
17. Hiskens, I.A. Analysis tool for power systems-contending with nonlinearities. *Proc. IEEE* **1995**, *83*, 1573–1587.
18. Sun, Q.; Yu, Y.X. Hyper-plane approximation of boundary of small signal stability region and its application. *J. Tianjin Univ.* **2008**, *41*, 647–652. (In Chinese)
19. Yang, S.; Liu, F.; Zhang, D.; Mei, A.W. Polynomial approximation of the small-signal stability region boundaries and its credible region in high-dimensional parameter space. *Int. Trans. Electr. Energy Syst*. **2013**, *23*, 784–801.
20. Jia, H.J.; Yu, X.D.; Cao, X.D. Impact of the exciter voltage limit to small signal stability region of a tree-bus power system. *Int. J. Electr. Power Energy Syst.* **2011**, *33*, 1598–1607.
21. Jia, H.J.; Yu, X.D.; Yu, Y.X.; Wang, C.S. Power system small signal stability region with time delay. *Int. J. Electr. Power Energy Syst.* **2008**, *30*, 16–22.
22. Li, G.Q.; Li, J.; Gao, S. Power system small signal stability region with saturation element considered. *Autom. Electr. Power Syst.* **2010**, *34*, 14–17. (In Chinese)
23. Pulgar, P.; Hector, A. *Wind Farm Model for Power System Stability Analysis*; The University of Illinois at Urbana-Champaign: Champaign, IL, USA, 2010.
24. Ash, R.; Ash, G. Numerical computation of root loci using the newton-raphson technique. *IEEE Trans. Autom. Control* **1968**, *13*, 576–582.
25. Saunders, P.T. *An Introduction to Catastrophe Theory*, 1st ed.; Cambridge University Press: New York, NY, USA, 1980; pp. 1–60.
26. Zeeman, E.C. *Catastrophe Theory*; Springer: Berlin/Heidelberg, Germany, 1976; pp. 1–83.
27. Robert, G. *Catastrophe Theory for Scientists and Engineers*; Wiley: New York, NY, USA, 1993; pp. 1–92.

28. Papacharalampous, A.E.; Vlahogianni, E.I. Modeling microscopic freeway traffic using cusp catastrophe theory. *IEEE Intell. Transp. Syst. Mag.* **2014**, *6*, 6–16.
29. Jones, D.D.; Walters, C.J. Catastrophe theory and fisheries regulation. *J. Fish. Res. Board Can*. **1976**, *33*, 2829–2833.
30. Qin, S.; Jiao, J.J.; Wang, S. A cusp catastrophe model of instability of slip-buckling slope. *Rock Mech. Rock Eng.* **2001**, *34*, 119–134.
31. Helbing, D.; Farkas, I.; Vicsek, T. Simulating dynamical features of escape panic. *Nature* **2000**, *407*, 487–490.
32. Sallam, A.A.; Dineley, J.L. Catastrophe theory as a tool for determining synchronous power system dynamic stability. *IEEE Trans. Power Appar. Syst.* **1983**, *102*, 622–630.
33. Wvong, M.D.; Mihirig, A.M. Catastrophe theory applied to transient stability assessment of power systems. *IEE Proc. Gener. Transm. Distrib.* **1986**, *133*, 314–318.
34. Mihirig, A.M.; Wvong, M.D. Transient stability analysis of multimachine power systems by catastrophe theory. *IEE Proc. Gener. Transm. Distrib.* **1989**, *136*, 254–258.
35. Mahmoud, G.A. Voltage stability analysis of radial distribution networks using catastrophe theory. *Gener. Transm. Distrib. IET* **2012**, *6*, 612–618.
36. Quan, Y.S.; Chen, J.; Li, W.; Zhang, X.D.; Peng, X.J.; Lao, G.Q. Methodology of forecasting the oil-immersed transformer over-hot fault tendency based on catastrophe theory. *Proc. CSEE* **2011**, *31*, 100–106. (In Chinese)
37. Zhou, H.Q.; Song, Z.P.; Wang, J.P.; Xue, Y. A review on dynamic equivalent methods for large scale wind farms. In Proceedings of the 2011 Asia-Pacific Power and Energy Engineering Conference (APPEEC 2011), Wuhan, China, 25–28 March 2011.
38. Kundur, P. *Power System Stability and Control*; McGraw-Hill: New York, NY, USA, 1994; pp. 700–705.
39. Hansen, A.D.; Jauch, C.; Sørensen, P.; Cutululis, N.; Jauch, C.; Blaabjerg, F. *Dynamic Wind Turbine Models in Power System Simulation Tool DIgSILENT*; The Risø National Laboratory: Roskilde, Denmark, 2003; pp. 1–82.
40. Anderson, P.M.; Fouad, A.A. *Power System Control and Stability*, 2nd ed.; Wiley: Southern Gate, UK, 2002; pp. 555–582.